



**The interplay between activity and filament flexibility
determines the emergent properties of active nematics**

Journal:	<i>Soft Matter</i>
Manuscript ID	SM-ART-10-2018-002202
Article Type:	Paper
Date Submitted by the Author:	29-Oct-2018
Complete List of Authors:	Joshi, Abhijeet; Brandeis University, Physics Putzig, Elias; Brandeis University, Martin A. Fisher School of Physics Baskaran, Aparna; Brandeis University, Physics Hagan, Michael; Brandeis University, Physics

The interplay between activity and filament flexibility determines the emergent properties of active nematics

Abhijeet Joshi, Elias Putzig, Aparna Baskaran,* and Michael F. Hagan†
Martin Fisher school of Physics, Brandeis University, Waltham, MA 02453, USA
 (Dated: November 28, 2018)

Active nematics are microscopically driven liquid crystals that exhibit dynamical steady states characterized by the creation and annihilation of topological defects. Motivated by differences between previous simulations of active nematics based on rigid rods and experimental realizations based on semiflexible biopolymer filaments, we describe a large-scale simulation study of a particle-based computational model that explicitly incorporates filament semiflexibility. We find that energy injected into the system at the particle scale preferentially excites bend deformations, reducing the apparent filament bend modulus. The emergent characteristics of the active nematic depend on activity and flexibility only through this activity-renormalized bend ‘modulus’, demonstrating that apparent values of material parameters, such as the Frank ‘constants’, depend on activity. Thus, phenomenological parameters within continuum hydrodynamic descriptions of active nematics must account for this dependence. Further, we present a systematic way to estimate these parameters from observations of deformation fields and defect shapes in experimental or simulation data.

I. INTRODUCTION

Active nematics are a class of non-equilibrium liquid crystalline materials in which the constituent particles transduce energy into stress and motion, driving orientationally inhomogeneous dynamical steady states characterized by generation, annihilation, and streaming of topological defects [1–7]. Being intrinsically far-from-equilibrium, active nematics enable developing materials with capabilities that would be thermodynamically forbidden in an equilibrium system. However, such applications require understanding how an active nematic’s macroscale material properties depend on the microscale features of its constituent nematogens.

The challenge in this task can be illustrated by considering the shape of a defect. Defects have been the subject of intense research in equilibrium nematics, since they must be eliminated for display technologies, and controlled for applications such as directed assembly and biosensing [8–10]. Theory and experiments [10–12] have shown that defect morphologies depend on the relative values of the bend and splay elastic moduli, k_{33} and k_{11} (Fig. 1a), defined in the Frank free energy density for a 2D nematic as $f_F = k_{11} (\nabla \cdot \hat{n})^2 + k_{33} (\hat{n} \times (\nabla \times \hat{n}))^2$ with \hat{n} the director field [13, 14]. Different experimental realizations of active nematics also exhibit variations in defect morphologies (*e.g.* Fig. 1c and Fig. 1d). However, relating these defect morphologies to material constants is much less straightforward than in equilibrium systems. Since moduli are an equilibrium concept, they cannot be rigorously defined in a non-equilibrium system such as an active nematic. If it is possible to define ‘effective moduli’ in active systems, there is currently no systematic way to measure them, and it is unclear whether and how they may depend on activity.

Computational and theoretical modeling could overcome these limitations. Symmetry-based hydrodynamic theories [15–17] have led to numerous insights about active nematics, including describing defect dynamics (*e.g.* [18–23]), induced flows in the suspending fluid (*e.g.* [24–26]), and how confinement in planar [27–30] and curved geometries [31–34] controls defect proliferation and dynamics. However, hydrodynamic theories cannot predict how material constants or emergent behaviors depend on the microscale properties of individual nematogens. Further, while simulations of active nematics composed of rigid rods [2, 35–37] have elucidated emergent morphologies, these models do not account for internal degrees of freedom available to flexible nematogens [1, 38, 39].

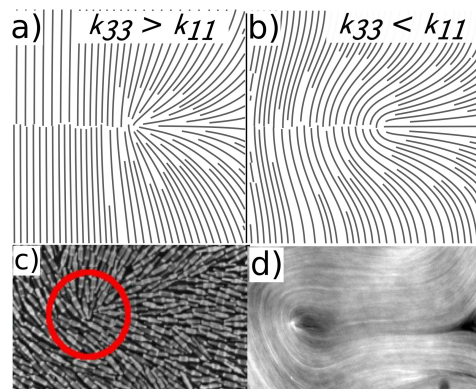


FIG. 1. (a,b) The equilibrium director field configuration near a $+\frac{1}{2}$ defect for (a) bend modulus larger than splay modulus $k_{33}/k_{11} = 3.4$, leading to pointed defects and (b) splay modulus larger than bend $k_{33}/k_{11} = 0.3$ leading to rounded defects. In each case the director field was calculated by numerically minimizing the Frank free energy around a separated $\pm\frac{1}{2}$ defect pair. (c,d) Typical defect morphologies observed in (c) a vibrated granular nematic [5] and (d) a microtubule-based active nematic [1, 40].

* email:aparna@brandeis.edu

† email:hagan@brandeis.edu

In this work, we perform large-scale simulations on a

model active nematic composed of semiflexible filaments, and determine how its emergent morphology depends on filament stiffness and activity. Fig. 2 shows representative simulation outcomes. We find that the intrinsic bending modulus of nematogens κ undergoes an apparent softening in an active nematic, according $\kappa_{\text{eff}} \sim \kappa/(f^a)^2$, where f^a is a measure of its activity. Furthermore, the characteristics of the active nematic texture — the defect density, magnitudes and characteristic scales of bend and splay deformations, the shape of motile $+\frac{1}{2}$ defects, and number fluctuations — depend on activity and rigidity only through the apparent nematogen rigidity κ_{eff} . Moreover, we show that one can define effective bend and splay moduli analogous to their equilibrium counterparts, but that the apparent bend modulus is proportional to κ_{eff} . This observation demonstrates that activity preferentially dissipates into particular modes within an active material, depending on the internal degrees of freedom of its constituent units. Further, these results suggest revisiting assumptions underlying existing hydrodynamic theories of active matter, since a microscopic model for an active fluid results in macroscopic properties that depend on activity in nontrivial ways, which cannot be simply described by an active stress. Finally, we present a method of parameterizing defect shapes, which enables estimating the relative magnitudes of apparent bend and splay constants from experimental observations of defects, and thus allows direct experimental testing of our prediction.

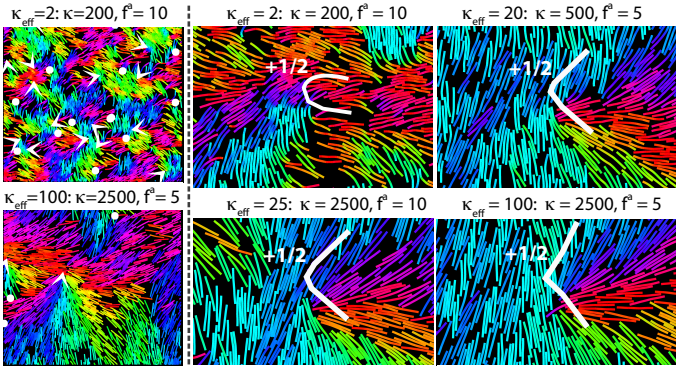


FIG. 2. A visual summary of how active nematic emergent properties depend on the activity parameter f^a and the filament modulus κ . The left panel in each row shows $1/16^{\text{th}}$ of the simulation box for indicated parameter values, with white arrows indicating positions and orientations of $+\frac{1}{2}$ defects and white dots indicating positions of $-\frac{1}{2}$ defects. Filament beads are colored according to the orientations of the local tangent vector. The right 4 panels are each zoomed in on a $+\frac{1}{2}$ defect, with indicated parameter values. The white lines are drawn by eye to highlight defect shapes. Animations of corresponding simulation trajectories are in [41]. The box size is $(840 \times 840\sigma^2)$ for all simulations in this work. Other parameters are $\tau_1 = 0.2\tau$ and $k_b = 300k_B T_{\text{ref}}/\sigma^2$.

II. METHODS

We seek a minimal computational model that captures the key material properties and symmetries of active nematics, namely extensile activity, nematic inter-particle alignment and semiflexibility. We model active filaments as semiflexible bead-spring polymers, each containing M beads of diameter σ , with flexibility controlled by a harmonic angle potential between successive bonds that sets the filament bending modulus κ . Activity is implemented as a force of magnitude f^a acting on each filament bead along the local tangent to the filament. To make activity nematic, the active force on every bead within a given filament reverses direction after a time interval chosen from a Poisson distribution with mean τ_1 . The Langevin equations governing the system dynamics were integrated using a modified version of LAMMPS [42]. The model combines features of recent models for polar self-propelled polymers [43] and the reversing rods approach to rigid active nematic rods [36].

Equations of motion and interaction potentials: We simulate the dynamics according to the following Langevin equation for each filament α and bead i (with filaments indexed by Greek letters, $\alpha = 1 \dots N$, and beads within a filament indexed in Roman, $i = 1 \dots M$):

$$m\ddot{\mathbf{r}}_{\alpha,i} = \mathbf{f}_{\alpha,i}^a - \gamma\dot{\mathbf{r}}_{\alpha,i} - \nabla_{\mathbf{r}_{\alpha,i}}U + \mathbf{R}_{\alpha,i}(t). \quad (1)$$

with m as the bead mass, $\mathbf{r}_{\alpha,i}$ as the bead position, f^a as the active force, U as the interaction potential which gives rise to the conservative forces, γ as the friction coefficient providing the damping and $\mathbf{R}_{\alpha,i}(t)$ as a delta-correlated thermal noise with zero mean and variance $\langle \mathbf{R}_{\alpha,i}(t) \cdot \mathbf{R}_{\beta,j}(t') \rangle = 4\gamma k_B T \delta_{\alpha,\beta} \delta_{i,j} \delta(t-t')$.

The interaction potential includes three contributions which respectively account for non-bonded interactions between all bead pairs, stretching of each bond, and the angle potential between each pair of neighboring bonds:

$$\begin{aligned} U(\{\mathbf{r}_{\alpha,i}\}) = & \frac{1}{2} \sum_{\alpha,\beta=1}^N \sum_{i,j=1}^M (1 - \delta_{\alpha,\beta} \delta_{i,j}) U_{\text{nb}}(|\mathbf{r}_{\beta,j} - \mathbf{r}_{\alpha,i}|) \\ & + \sum_{\alpha=1}^N \sum_{i=2}^M U_s(|\mathbf{r}_{\alpha,i} - \mathbf{r}_{\alpha,i-1}|) \\ & + \sum_{\alpha=1}^N \sum_{i=3}^M U_{\text{angle}}(\theta_{\alpha,i,i-1,i-2}) \end{aligned} \quad (2)$$

with $\theta_{\alpha,i,j,k}$ the angle made by the bead triplet $\{i, j, k\}$ on filament α . The non-bonded interactions account for steric repulsion and are modeled with the Weeks-Chandler-Anderson potential[44]

$$U_{\text{nb}}(r) = 4\epsilon \left((\sigma/r)^{12} - (\sigma/r)^6 + 1/4 \right) \Theta(2^{1/6}\sigma - r) \quad (3)$$

with ϵ controlling the strength of steric repulsion and $\Theta(x)$ the Heaviside function specifying the cutoff. Bond stretching is controlled by a FENE potential [45]

$$U_s(r) = -1/2k_b R_0^2 \ln \left(1 - (r/R_0)^2 \right) \quad (4)$$

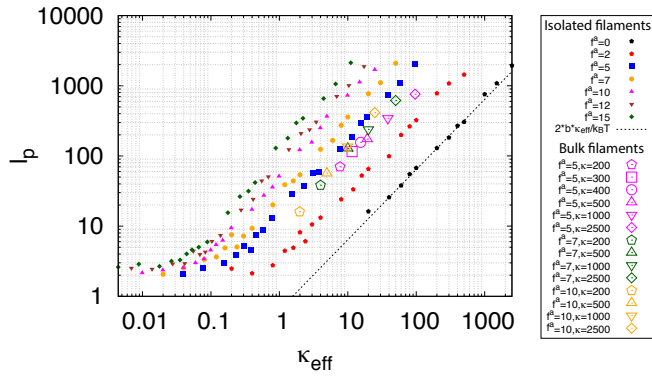


FIG. 3. Effective persistence length l_p estimated from the spectrum of filament tangent fluctuations in bulk active nematics (large open symbols), and isolated chains (small solid symbols). The dashed line shows the expected scaling for an isolated equilibrium polymer ($f^a = 0$), $l_p = 2b\kappa_{\text{eff}}/k_B T$, and the legend shows the value of f^a for all systems, and κ for the bulk simulations. Other parameters are $\tau_1 = \tau$ and $k_b = 30k_B T_{\text{ref}}/\sigma^2$.

with bond strength k_b and maximum bond length R_0 . The angle potential is given by

$$U_{\text{angle}}(\theta) = \kappa (\theta - \pi)^2 \quad (5)$$

where κ is the filament bending modulus.

Finally, activity is modeled as a propulsive force on every bead directed along the filament tangent toward its head. To render the activity nematic, the head and tail of each filament are switched at stochastic intervals so that the force direction on each bead rotates by 180 degrees. In particular, the active force has the form, $\mathbf{f}_{\alpha,i}^a(t) = \eta_\alpha(t) f^a \mathbf{t}_{\alpha,i}$, where f^a parameterizes the activity strength, and $\eta_\alpha(t)$ is a stochastic variable associated with filament α that changes its values between 1 and -1 on Poisson distributed intervals with mean τ_1 , so that τ_1 controls the reversal frequency.

Simulations and parameter values: Since we are motivated by systems sufficiently large that boundary effects are negligible (*e.g.* Ref. [2]), we performed simulations in a $A = 840 \times 840\sigma^2$ periodic simulation box, with $N = 19404$ filaments, each with $M = 20$ beads, so that the packing fraction $\phi = MN\sigma^2/A \approx 0.55$. Fixing all other model parameters, we varied the filament stiffness, $\kappa \in [10^2, 10^4]k_B T_{\text{ref}}$ and the magnitude of the active force, $f^a \in [5, 30]k_B T_{\text{ref}}/\sigma$, where the units are set by the thermal energy at a reference state $k_B T_{\text{ref}}$, and the filament diameter σ . Time is measured in units of $\tau = \sqrt{m\sigma^2/k_B T_{\text{ref}}}$. We set mass of the each bead to $m = 1$, the damping coefficient to $\gamma = 2$, and the temperature to $T = 3.0k_B T_{\text{ref}}$. With these parameters inertia is non-negligible. In the future, we plan to systematically investigate the effect of damping. We set the repulsion parameter $\varepsilon = k_B T_{\text{ref}}$ (the results are insensitive to the value of ε provided it is sufficiently high to avoid filament overlap), and used a time step of $\delta t = 10^{-3}\tau$.

In the FENE bond potential, R_0 is set to 1.5σ and $k_b = 300k_B T_{\text{ref}}/\sigma^2$ for the simulations reported in the main text (except in Fig. 3). These parameters lead to a mean bond length of $b \approx 0.84\sigma$, which ensures that filaments are non-penetrable for the parameter space explored in this work. We have fixed the filament length at $M = 20$ beads, so $L = (M - 1)b$ is the mean filament length. Varying M does not change the scaling of observables, although it shifts properties such as the defect density since the total active force per filament goes as $f^a M$. Also, the maximum persistence length above which scaling laws fail is also proportional to M (see Results). In the semiflexible limit, the stiffness κ in the discrete model is related to the continuum bending modulus $\tilde{\kappa}$ as $\kappa \approx \tilde{\kappa}/2b$, and thus the persistence length is given by $l_p = 2b\kappa/k_B T$.

We performed two sets of simulations. Initially, we set the FENE bond strength $k_b = 30k_B T_{\text{ref}}/\sigma^2$ and $\tau_1 = \tau$. However, for these parameters we discovered that interpenetration of filaments becomes possible at large propulsion velocities, thus limiting the simulations to $f^a \leq 10$. To enable investigating higher activity values, we therefore performed a second set of simulations (those reported in Figs. 4-7 of the main text) with higher FENE bond strength, $k_b = 300k_B T_{\text{ref}}/\sigma^2$ and shorter reversal timescale $\tau_1 = 0.2$, with $\kappa \in [100, 10000]k_B T_{\text{ref}}$. This enables simulating activity values up to $f^a \leq 30$.

The shorter reversal timescale was needed to keep the system in the nematic regime at large f^a . When the product $f^a \tau$ exceeds a characteristic collision length scale the self-propulsion becomes polar in nature and model is no longer a good description of an active nematic. In particular, the filaments behave as polar self-propelled rods, as evidenced by the formation of polar clusters [46–50]. Interestingly, increasing k_b increases the rate of defect formation and decreases the threshold value of $f^a \tau$ above which phase separation occurs. We monitored the existence of phase separation by measuring local densities within simulation boxes (see [41]). We found no significant phase separation (except on short scales, see below) or formation of polar clusters for any of the simulations described here, indicating the systems were in the nematic regime. Within the nematic regime, increasing k_b does not qualitatively change results or scaling relations, although it does quantitatively shift properties such as the defect density. Additional plots for the simulation set with $k_b = 30$ are shown in the SI [41].

Initialization: We initialized the system by first placing the filaments in completely extended configurations (all bonds parallel and all bond lengths set to b), on a rectangular lattice with filaments oriented along one of the lattice vectors. We then relaxed the initial configuration for $10^4 \tau$, where $\tau = \sqrt{m\sigma^2/k_B T_{\text{ref}}}$, before performing production runs of $\sim 4 \times 10^4 \tau$. The equilibration time of $10^4 \tau$ was chosen based on the fact that in all simulated systems the defect density had reached steady state by this time. We also confirmed that other observables of interest have reached steady state at this time. In the limit

of high stiffness or low activity, the unphysical crystalline initial condition did not relax on computationally accessible timescales. In these cases, we used an alternative initial configuration, with filaments arranged into four rectangular lattices, each placed in one quadrant of the simulation box such that adjacent (non-diagonal) lattices were orthogonal.

III. RESULTS AND DISCUSSION.

To understand how the interplay between filament flexibility and activity determines the texture of an active nematic, we analyzed our simulation results using multiple metrics for the deformations in nematic order.

Before reporting these results, let us first consider the basic physics governing the emergent phenomenology in our system. Deforming a nematogen causes an elastic stress that scales $\sim \kappa$, the filament bending modulus. This elastic stress must be balanced by stresses arising from interparticle collisions. These collisional stresses have two contributions. First there are the passive collisional stresses, which are $\mathcal{O}(1)$ in our units (as we have chosen the thermal energy and the particle size σ as the energy and length scales). Then there are active collisional stresses that arise due to the self-replenishing active force of magnitude f^a acting on each monomer. The active collisional stress will scale as $\nu_{\text{coll}}\Delta p_{\text{coll}}$, i.e., the collision frequency times the momentum transfer at each collision. Both the collision frequency and momentum transfer will scale with the self-propulsion velocity [51], which in our model is set by f^a . Thus, the collisional stresses will scale $\sim (1 + (f^a)^2)$. So, the system properties will be controlled by a parameter which measures the ratio of elastic to collisional stresses, $\kappa_{\text{eff}} \equiv \kappa / (1 + (f^a)^2)$.

Persistence length: To test this scaling, we measured the tangent fluctuations of individual filaments within our computational active nematic. We then determined the effective persistence length from the Fourier spectrum of these fluctuations (see [41] section S4 and Fig. S2). Fig. 3 shows estimated persistence lengths over a range of filament bending modulus values $\kappa \in (200, 2500)$, and activity parameter values $f^a \in (5, 10)$ from two sets of simulations: isolated chains (small solid symbols) and chains from the bulk active nematic (large open symbols). Note that the result for an isolated equilibrium polymer ($f^a = 0$, \blacklozenge symbols) perfectly matches the expected relationship $l_p = 2b\kappa_{\text{eff}}/k_B T$. For the bulk active chains we observe data collapse over all of these parameters when the persistence length is plotted as a function of κ_{eff} , with persistence length scaling as $l_p \sim \kappa_{\text{eff}}$. In contrast, the effective persistence length for isolated active chains does not exhibit data collapse; the persistence length scales linearly with κ but exhibits a different dependence on activity. This result supports the proposal that the apparent softening of filaments in bulk active nematics arises due to inter-chain collisions.

Note that we restrict the analysis to $f^a \geq 5$ because

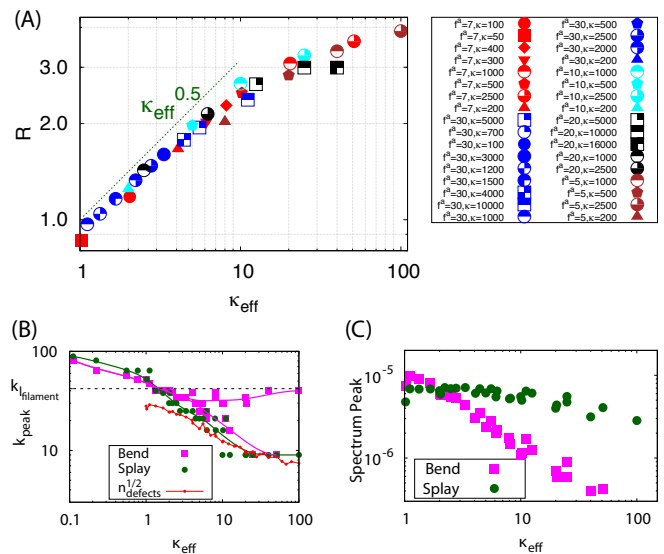


FIG. 4. Analysis of splay and bend deformations at steady state: (A) The ratio of splay and bend deformations, $R = \langle \int d^2\mathbf{r} D_{\text{splay}}(\mathbf{r}) \rangle / \langle \int d^2\mathbf{r} D_{\text{bend}}(\mathbf{r}) \rangle$ as a function of the effective bending rigidity, $\kappa_{\text{eff}} = \kappa / (1 + (f^a)^2)$. (B) The wavenumbers corresponding to peaks k_{peak} in bend (■ symbols) and splay (● symbols) power spectra, and the inverse defect spacing, $\sqrt{\langle n_{\text{defect}} \rangle}$ (● symbols) as functions of κ_{eff} . The predominant scale of splay deformations transitions from the individual filament scale (k_{filament} , dashed line) at low κ_{eff} to the defect spacing scale at high κ_{eff} . Bend spectra exhibit two peaks, corresponding to filament and defect-spacing scales, for high κ_{eff} . (C) The maximum magnitude of the power spectra, showing that splay is insensitive to κ_{eff} while bend deformations decrease in magnitude until the effective rigidity exceeds the filament length. Other parameters are $\tau_1 = 0.2\tau$ and $k_b = 300k_B T_{\text{ref}}/\sigma^2$.

the system loses nematic order for smaller activity values (see Fig. S5C [41] and ‘Comparison with Equilibrium’ below). The results in Fig. 3 were performed on our initial data set with $\tau_1 = \tau$ and $k_b = 30k_B T_{\text{ref}}/\sigma^2$ and thus are limited to $f^a \leq 10$ (see Methods).

We now test whether the arguments proposed above can describe the collective behaviors of an active nematic, using several metrics for deformations in the nematic order: the distribution of energy in splay and bend deformations, defect shape, defect density, and number fluctuations. As shown in Figs. 4-7, all of these quantities depend on bending rigidity and activity only through the combination κ_{eff} . We performed the analysis of active nematics textures (described next) on the second parameter set with $\tau_1 = 0.2\tau$ and $k_b = 300k_B T_{\text{ref}}/\sigma^2$, which allowed $f^a \leq 30$.

Splay and Bend deformations: We first determine whether it is possible to define quantities analogous to splay and bend moduli in an active nematic. We emphasize that moduli cannot be rigorously defined in a non-equilibrium system, but we will see that the relative amounts of energy in bend and splay deformations, and

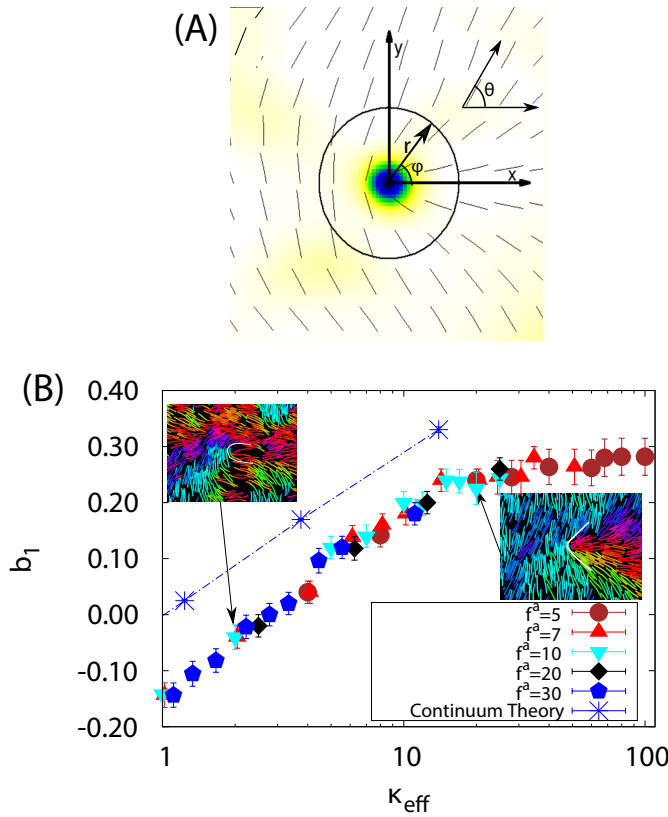


FIG. 5. Defect shape depends on the effective bending rigidity. (A) Schematic showing the defect-centered coordinate system defined in the text, with azimuthal angle ϕ and director angle $\theta(r, \phi)$. Note that the x -axis is chosen along the orientation vector of the $+1/2$ defect given by the angle θ'_0 defined in the SI [41]. (B) Mode of defect shape parameter b_1 for $+1/2$ defects as a function of κ_{eff} for $f^a \in [7, 30]$ and $\kappa \in [100, 10000]$, with $b_1(r)$ values evaluated at a radial distance $r = 12.6\sigma$ from the defect core. The dashed line and blue asterisk symbols show values of b_1 calculated for isolated defects from equilibrium continuum elastic theory, with the ratio of bend and splay moduli k_{33}/k_{11} for each κ_{eff} set according to the measured ratio R of bend and splay deformations in Fig. 4. Images of defects at two indicated parameter sets are shown. Other parameters are $\tau_1 = 0.2\tau$ and $k_b = 300k_B T_{\text{ref}}/\sigma^2$.

all other steady-state properties of an active nematic, can be described by ‘effective moduli’ if the effect of activity is accounted for.

In a 2D nematic, any arbitrary deformation of the director field can be decomposed into a bend deformation $\mathbf{d}_{\text{bend}} = (\hat{\mathbf{n}}(\mathbf{r}) \times (\nabla \times \hat{\mathbf{n}}(\mathbf{r})))$ and a splay deformation $d_{\text{splay}} = (\nabla \cdot \hat{\mathbf{n}}(\mathbf{r}))$. We define associated strain energy densities $D_{\text{bend}} = \rho S^2 |\mathbf{d}_{\text{bend}}|^2$ and $D_{\text{splay}} = \rho S^2 d_{\text{splay}}^2$, which measure how the system’s elastic energy distributes into the two linearly independent deformation modes. The prefactors of density ρ and order S allow the definitions to be valid in regions such as defect cores and voids that occur in the particle simulations.

To compare the splay and bend deformations to their

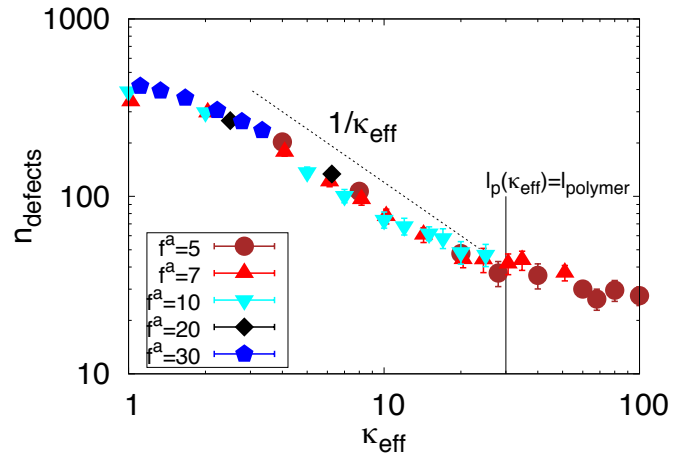


FIG. 6. The average number of defects n_{defect} observed in steady states as a function of κ_{eff} , for activity parameter values $f^a \in [5, 30]$ and $\kappa \in [100, 3000]$. Other parameters are $\tau_1 = 0.2\tau$ and $k_b = 300k_B T_{\text{ref}}/\sigma^2$.

form in an equilibrium nematic, let us consider the ratio of total strain energy in splay deformations to those in bend, $R = \langle \int d^2\mathbf{r} D_{\text{splay}}(\mathbf{r}) \rangle / \langle \int d^2\mathbf{r} D_{\text{bend}}(\mathbf{r}) \rangle$. In equilibrium, equipartition requires that this ratio satisfy $R_{\text{eq}} = k_{33}/k_{11}$. In our simulations, we observe that R depends strongly on activity; however, the data for all parameter sets collapses when plotted as a function of the effective filament bend modulus κ_{eff} . This result is consistent with the concept of effective moduli, but shows that their values depend on activity.

To understand why the apparent modulus values depend on activity, we analyzed the power spectra associated with these strain energies (Fig. S4 in [41]). The power spectra exhibit two features: 1) Fig. 4b shows that for the smallest simulated effective rigidity, $\kappa_{\text{eff}} = 2$, the peak of the power spectrum k_{peak} is on the filament scale, indicating that most deformation energy arises due to bending of individual filaments. But for all higher values of κ_{eff} , a peak arises at the defect spacing scale, indicating that the defect density controls the texture in this active nematic. 2) Fig. 4c shows the magnitude of the power spectrum at the characteristic scale k_{peak} . The splay energy density is nearly independent of the effective filament stiffness, while the amount of bend decreases linearly with κ_{eff} for $\kappa_{\text{eff}} \lesssim \kappa_{\text{eff}}^{\text{max}}$, where $\kappa_{\text{eff}}^{\text{max}} \approx 30$ is the point at which the effective persistence length of the filaments is equal to their contour length. This observation demonstrates that energy injected into the system at the microscale due to activity preferentially dissipates into bend modes.

Defect Shape: Let us now consider a striking feature of the texture of an active nematic, the shape of a $+1/2$ defect. A quantitative descriptor of defect shape can be developed as follows. We choose a coordinate system with its origin at the center of the defect core, with the x -axis pointing along the defect orientation (see Fig. 5a).

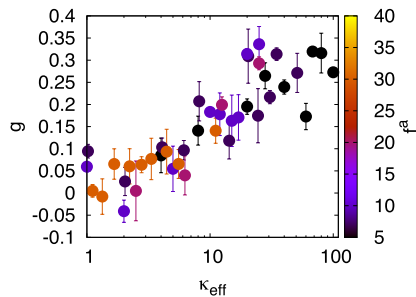


FIG. 7. Giant number fluctuations (GNFs) depend on the effective bending rigidity. The fluctuation scaling exponent g is plotted as a function of κ_{eff} , where we determined g by fitting the dependence of fluctuations on subsystem size for each parameter set to the form $\Delta N/\sqrt{N} = aN^g$ over the range $N \leq 10^4$. Note that a value of $g = 0$ corresponds to equilibrium-like fluctuations, while $g = 0.5$ would correspond to $\Delta N \sim N$. The color of each point indicates the value of f^a according to the color bar on the right. Other parameters are $\tau_1 = 0.2\tau$ and $k_b = 300k_B T_{\text{ref}}/\sigma^2$.

We work in polar coordinates, with r the radial distance from the defect core and ϕ as the azimuthal angle with respect to the x -axis. We define θ as the angle of the director field with respect to the x -axis. At any position, we can then express $\theta(r, \phi)$ as a Fourier expansion in $\phi \in \{-\pi : \pi\}$.

$$\theta(r, \phi) = \frac{1}{2}\phi + \sum_n a_n \cos(n\phi) + b_n \sin(n\phi). \quad (6)$$

However, in practice truncating the expansion after the first sin term approximates the shape of a $+\frac{1}{2}$ defect well, so the descriptor simplifies to $\theta_{+\frac{1}{2}}(r, \phi) \approx \frac{1}{2}\phi + b_1(r)\sin(\phi)$, and the result is insensitive to r provided the measurement is performed outside of the defect core (see Fig. S10 [41]). Thus, the parameter b_1 uniquely describes the defect shape; in particular, larger values of b_1 correspond to pointier defects. Note that Zhang et al. [12] and Cortese et al. [22] recently proposed similar approaches to characterizing defect shapes. An advantage of our approach is that the shape can be described by a single number, b_1 .

Fig. 5B shows the mode of b_1 calculated from defects within our simulations depends only on κ_{eff} , thus demonstrating that defect shape is controlled by the apparent bending rigidity. Moreover, b_1 increases logarithmically with κ_{eff} ; i.e., defects become more pointed as the bending rigidity increases, consistent with the previous observations of highly pointed defects in rigid rod simulations [2, 35, 52].

Defect Density: We next consider a well-studied property of an active nematic, the steady-state defect density [19, 24, 28, 53]. Fig. 6 shows defect density collapses onto a single curve when plotted as a function of κ_{eff} , and scales roughly as $1/\kappa_{\text{eff}}$ under parameter values for which the apparent persistence length lies between the monomer scale and filament contour length,

$1.5 \lesssim \kappa_{\text{eff}} \lesssim \kappa_{\text{eff}}^{\text{max}}$. We observe the same scaling for our other data set (Fig. S1 [41]). Hydrodynamic theories such as [19, 24, 28, 53] predict that the defect density scales as α/K , where α is the measure of active stress in the hydrodynamic theories and K is a Frank elastic constant. The scaling collapse observed in our simulations indicates that these hydrodynamic parameters are directly related to their microscopic analogs, namely the filament elastic constant κ and the collisional active stress $\sim (1 + (f^a)^2)$. Note that we could not measure defect densities in systems with both extremely high activity and high bare bending rigidity ($f^a \geq 20$ and $\kappa \gtrsim 5000$) because our defect detection algorithm breaks down (see section S8 of [41]).

Number fluctuations: Finally, previous work has shown that active nematics are susceptible to phase separation [36, 54–56] and giant number fluctuations (GNFs) [5, 54, 57–59]. We find that flexibility suppresses phase separation except at molecular scales (Fig. S8 [41]), but that number fluctuations are governed by the apparent modulus. We monitored number fluctuations by measuring the number of pseudoatoms within square subsystems with side lengths ranging from 20σ to 840σ . At equilibrium, in a region containing on average N particles the standard deviation of the number of particles ΔN scales as $\Delta N \sim \sqrt{N}$, while previous studies of active nematics have identified higher scaling, as large as $\Delta N \sim N$. Fig. S9 [41] shows measured number fluctuations for different values of the effective bending modulus. We see that for small $\kappa_{\text{eff}} = 2$ the result is constant with subsystem size, indicating equilibrium-like fluctuations, but the slope increases larger effective modulus values, indicating a progression toward GNFs. At all κ_{eff} the fluctuations are eventually suppressed on scales comparable to the defect spacing ($N \gtrsim 10^4$), at which scale the system is essentially isotropic, consistent with Narayan et al. [5].

To determine the dependence on κ_{eff} , we fit the data for each simulation in the range $N \leq 10^4$ to the form aN^g , so that $g = 0$ indicates equilibrium-like fluctuations and $g = 0.5$ would indicate linear scaling of fluctuations with system size. As shown in Fig. 7, g increases with κ_{eff} , with $g = 0$ for small κ_{eff} and $g \approx 0.3$ for the largest effective bending rigidity values investigated; i.e. $\Delta N \sim N^{0.8}$. The fact that $g < 0.5$ for the parameters we consider may reflect suppression of fluctuations even for $N < 10^4$. Importantly, estimated values of g at different f^a and κ collapse onto a single function of κ_{eff} , consistent with the observations of the other characteristics of an active nematic shown above.

Comparison with equilibrium: For small values of κ_{eff} , the bend/splay ratio roughly in our model active nematic scales as $R \sim \kappa_{\text{eff}}^{1/2}$ (Fig. 4). This differs from the scaling of an equilibrium nematic, where the moduli scale as $k_{33} \sim \kappa$ and $k_{11} \sim \kappa^{1/3}$ [60, 61], giving $R_{\text{eq}} \sim \kappa^{2/3}$. We confirmed this scaling by calculating the equilibrium moduli for our system (Fig. S5 [41]) using the free energy perturbation technique of [62]. Analysis of simulation trajectories suggests that the difference in scal-

ing arises because the active systems have much higher nematic order than the equilibrium systems (when compared at the same values of effective bending rigidity). In an equilibrium system, increasing the filament flexibility decreases order, resulting in a transition from the nematic to isotropic phase as κ decreases below 5 at the density used in our simulations [63]. In contrast, the active systems remain deep within the nematic phase ($S \gtrsim 0.8$) for all parameter sets (Fig. S5c in [41]). We empirically found that normalizing the bend-splay ratio by the degree of order, using the form R/S^2 , roughly collapses the equilibrium and active results onto a single curve (Fig. S5b [41]). Although we cannot rationalize the form of the normalization, this result implies that the differences in scaling between active and equilibrium cases arise from the increased nematic order in the active simulations.

Returning to the defect shape measurements, the dashed line in Fig. 5B shows the defect shape parameter values b_1 calculated by minimizing the continuum Frank free energy for an equilibrium system containing a separated pair of $+\frac{1}{2}$ and $-\frac{1}{2}$ defects. Here we have fixed the continuum modulus k_{11} and varied k_{33} so that $R_{\text{eq}} = \frac{k_{33}}{k_{11}}$ matches the value obtained from our microscopic simulations at the corresponding value of effective stiffness: $R_{\text{eq}}(k_{33}) = R(\kappa_{\text{eff}})$. Although the equilibrium b_1 values are shifted above the simulation results, consistent with the discrepancy in R between the active and passive systems described above, we observe the same scaling with bending rigidity in the continuum and simulation results. Thus, the defect shape measurement provides a straightforward means to estimate effective moduli in simulations or experiments on active nematics.

IV. CONCLUSIONS.

In active materials, energy injected at the particle scale undergoes an inverse cascade, manifesting in collective spatiotemporal dynamics at larger scales. The nature of this emergent behavior depends crucially on which modes

the active energy dissipates into. Our simulations show that activity within a dry active nematic preferentially dissipates into bend modes, thus softening the apparent bend modulus. Consequently, the value of the apparent bend modulus depends strongly on activity. However, we show that once this dependence on activity is accounted for, this effective modulus dictates all collective behaviors that we investigated — the relative amounts of bend and splay, defect density, defect shape, and giant number fluctuations. The dependence of multiple characteristics on this single parameter suggests that material properties such as apparent moduli can be meaningfully assessed in an active nematic and related to their values at equilibrium, provided their dependence on activity is accounted for. Finally, our technique to parameterize defect shapes allows estimating the relative magnitudes of these effective moduli in any experimental or computational system that exhibits defects.

Experimental confirmation of the predicted dependence of effective bend and splay moduli on activity: After a preprint of our manuscript first appeared, Ref. [64] presented elegant experimental results confirming that the ratio of apparent bend and splay moduli depend on activity as predicted here.

CONFLICTS OF INTEREST

There are no conflicts to declare.

ACKNOWLEDGMENTS

This work was supported by the Brandeis Center for Bioinspired Soft Materials, an NSF MRSEC, DMR-1420382 (AJ,EP,AB,MFH) and NSF DMR-1149266 (AB). Computational resources were provided by NSF XSEDE computing resources (MCB090163, Stampede) and the Brandeis HPCC which is partially supported by DMR-1420382.

-
- [1] T. Sanchez, D. T. N. Chen, S. J. Decamp, M. Heymann and Z. Dogic, *Nature*, 2012, **491**, 431–434.
 - [2] S. J. DeCamp, G. S. Redner, A. Baskaran, M. F. Hagan and Z. Dogic, *Nat. Mater.*, 2015, **14**, 1110 – 1115.
 - [3] C. Peng, T. Turiv, Y. Guo, Q.-H. Wei and O. D. Lavrentovich, *Science*, 2016, **354**, 882–885.
 - [4] S. Zhou, A. Sokolov, O. D. Lavrentovich and I. S. Aranson, *Proc. Natl. Acad. Sci. U. S. A.*, 2014, **111**, 1265–1270.
 - [5] V. Narayan, S. Ramaswamy and N. Menon, *Science*, 2007, **317**, 105–8.
 - [6] V. Narayan, N. Menon and S. Ramaswamy, *J. Stat. Mech: Theory Exp.*, 2006, **2006**, P01005.
 - [7] G. Duclos, C. Erlenkämper, J.-F. Joanny and P. Silberzan, *Nature Physics*, 2017, **13**, 58.
 - [8] D. J. Broer, *Nat. Mater.*, 2010, **9**, 99–100.
 - [9] I.-h. Lin, D. S. Miller, P. J. Bertics, C. J. Murphy, J. J. de Pablo and N. L. Abbott, *Science*, 2011, **332**, 1297–1300.
 - [10] M. Kleman, *Rep. Prog. Phys.*, 1989, **52**, 555–654.
 - [11] S. Zhou, S. V. Shiyankovskii, H.-S. Park and O. D. Lavrentovich, *Nat. Commun.*, 2017, **8**, 14974.
 - [12] R. Zhang, N. Kumar, J. L. Ross, M. L. Gardel and J. J. de Pablo, *Proc. Natl. Acad. Sci. U. S. A.*, 2018, **115**, E124–E133.
 - [13] F. C. Frank, *Discuss. Faraday Soc.*, 1958, **25**, 19.
 - [14] C. W. Oseen, *Trans. Faraday Soc.*, 1933, **29**, 883–899.
 - [15] R. A. Simha and S. Ramaswamy, *Phys. Rev. Lett.*, 2002, **89**, 058101.

- [16] M. C. Marchetti, J. F. Joanny, S. Ramaswamy, T. B. Liverpool, J. Prost, M. Rao and R. A. Simha, *Rev. Mod. Phys.*, 2013, **85**, 1143–1189.
- [17] S. Ramaswamy, *Annu. Rev. Condens. Matter Phys.*, 2010, **1**, 323–345.
- [18] L. Giomi, M. J. Bowick, X. Ma and M. C. Marchetti, *Phys. Rev. Lett.*, 2013, **110**, 228101.
- [19] L. Giomi, M. J. Bowick, P. Mishra, R. Sknepnek and M. Cristina Marchetti, *Phil. Trans. R. Soc. A*, 2014, **372**, 20130365–20130365.
- [20] A. Doostmohammadi, T. N. Shendruk, K. Thijssen and J. M. Yeomans, *Nat. Comm.*, 2017, **8**, 15326.
- [21] A. U. Oza and J. Dunkel, *New J. Phys.*, 2016, **18**, 093006.
- [22] D. Cortese, J. Eggers and T. B. Liverpool, *Phys. Rev. E*, 2018, **97**, 022704.
- [23] T. N. Shendruk, K. Thijssen, J. M. Yeomans and A. Doostmohammadi, *Physical Review E*, 2018, **98**, 010601.
- [24] S. P. Thampi, R. Golestanian and J. M. Yeomans, *EPL (Europhysics Letters)*, 2014, **105**, 18001.
- [25] L. Giomi, *Phys. Rev. X*, 2015, **5**, 031003.
- [26] L. M. Lemma, S. J. Decamp, Z. You, L. Giomi and Z. Dogic, *arXiv preprint arXiv:1809.06938*, 2018.
- [27] T. N. Shendruk, A. Doostmohammadi, K. Thijssen and J. M. Yeomans, *Soft Matter*, 2017, **13**, 3853–3862.
- [28] M. M. Norton, A. Baskaran, A. Opathalage, B. Langeslay, S. Fraden, A. Baskaran and M. F. Hagan, *Phys. Rev. E*, 2018, **97**, 012702.
- [29] T. Gao, M. D. Betterton, A.-S. Jhang and M. J. Shelley, *Phys. Rev. Fluids*, 2017, **2**, 093302.
- [30] P. Guillamat, J. Ignés-Mullol and F. Sagués, *Nature communications*, 2017, **8**, 564.
- [31] F. C. Keber, E. Loiseau, T. Sanchez, S. J. DeCamp, L. Giomi, M. J. Bowick, M. C. Marchetti, Z. Dogic and A. R. Bausch, *Science*, 2014, **345**, 1135–1139.
- [32] R. Zhang, Y. Zhou, M. Rahimi and J. J. De Pablo, *Nat. Comm.*, 2016, **7**, 13483.
- [33] P. W. Ellis, D. J. G. Pearce, Y.-W. Chang, G. Goldsztein, L. Giomi and A. Fernandez-Nieves, *Nature Physics*, 2017, **14**, 85.
- [34] F. Alaïmo, C. Köhler and A. Voigt, *Sci. Rep.*, 2017, **7**, 5211.
- [35] T. Gao, R. Blackwell, M. A. Glaser, M. D. Betterton and M. J. Shelley, *Phys. Rev. Lett.*, 2015, **114**, 048101.
- [36] X.-q. Shi and Y.-q. Ma, *Nat. Comm.*, 2013, **4**, 3013.
- [37] S. Henkes, M. C. Marchetti and R. Sknepnek, *Physical Review E*, 2018, **97**, 042605.
- [38] Y. Sumino, K. H. Nagai, Y. Shitaka, D. Tanaka, K. Yoshikawa, H. Chaté and K. Oiwa, *Nature*, 2012, **483**, 448.
- [39] P. Guillamat, J. Ignés-Mullol and F. Sagués, *Proc. Natl. Acad. Sci. U. S. A.*, 2016, **113**, 5498–5502.
- [40] Image provided by Linnea Metcalf, Achini Opathalage and Zvonimir Dogc and used with their permission.
- [41] Supplementary material to this paper is provided at [URL].
- [42] S. Plimpton, *J. Comput. Phys.*, 1995, **117**, 1–19.
- [43] K. R. Prathyusha, S. Henkes and R. Sknepnek, *Phys. Rev. E*, 2018, **97**, 022606.
- [44] J. D. Weeks, D. Chandler and H. C. Andersen, *J. Chem. Phys.*, 1971, **54**, 5237–5247.
- [45] K. Kremer and G. S. Grest, *J. Chem. Phys.*, 1990, **92**, 5057–5086.
- [46] F. Peruani, A. Deutsch and M. Bär, *Phys. Rev. E*, 2006, **74**, 030904.
- [47] S. R. McCandlish, A. Baskaran and M. F. Hagan, *Soft Matter*, 2012, **8**, 2527–2534.
- [48] S. Weitz, A. Deutsch and F. Peruani, *Phys. Rev. E*, 2015, **92**, 012322.
- [49] F. Ginelli, F. Peruani, M. Bär and H. Chaté, *Phys. Rev. Lett.*, 2010, **104**, 184502.
- [50] F. Peruani, J. Starruß, V. Jakovljevic, L. Søgaard-Andersen, A. Deutsch and M. Bär, *Phys. Rev. Lett.*, 2012, **108**, 098102.
- [51] A. Baskaran and M. C. Marchetti, *Phys. Rev. Lett.*, 2008, **101**, 268101.
- [52] X. qing Shi, H. Chaté and Y. qiang Ma, *New J. Phys.*, 2014, **16**, 035003.
- [53] E. Putzig, G. S. Redner, A. Baskaran and A. Baskaran, *Soft Matter*, 2015, **12**, 1–5.
- [54] S. Mishra and S. Ramaswamy, *Phys. Rev. Lett.*, 2006, **97**, 090602.
- [55] S. Ngo, A. Peshkov, I. S. Aranson, E. Bertin, F. Ginelli and H. Chaté, *Phys. Rev. Lett.*, 2014, **113**, 038302.
- [56] E. Putzig and A. Baskaran, *Phys. Rev. E*, 2014, **90**, 042304.
- [57] S. Ramaswamy, R. A. Simha and J. Toner, *Europhys. Lett.*, 2003, **62**, 196–202.
- [58] H. Chaté, F. Ginelli and R. Montagne, *Phys. Rev. Lett.*, 2006, **96**, 180602.
- [59] H. P. Zhang, A. Be'er, E.-L. Florin and H. L. Swinney, *Proc. Natl. Acad. Sci. U. S. A.*, 2010, **107**, 13626–13630.
- [60] J. V. Selinger and R. F. Bruinsma, *Phys. Rev. A*, 1991, **43**, 2910–2921.
- [61] M. Dijkstra and D. Frenkel, *Phys. Rev. E*, 1995, **51**, 5891–5898.
- [62] A. A. Joshi, J. K. Whitmer, O. Guzmán, N. L. Abbott and J. J. de Pablo, *Soft Matter*, 2014, **10**, 882–893.
- [63] Note that this 2D system with soft-core interactions should exhibit quasi-long-range order in the nematic phase [65–67], and thus S decays with system size. Since we are interested in the degree of order on the scale of typical bend and splay fluctuations, we report S values measured within regions of size $10 \times 10\sigma^2$ (see [41]).
- [64] N. Kumar, R. Zhang, J. J. de Pablo and M. L. Gardel, *Science Advances*, 2018, **4**, eaat7779.
- [65] J. P. Straley, *Phys. Rev. A*, 1971, **4**, 675–681.
- [66] D. Frenkel and R. Eppenga, *Phys. Rev. A*, 1985, **31**, 1776–1787.
- [67] J. M. Kosterlitz and D. J. Thouless, *J. Phys. C: Solid State Phys.*, 1973, **6**, 1181.